Nanoscale

PAPER

View Article Online
View Journal | View Issue

Cite this: *Nanoscale*, 2016, **8**, 9791

An enzyme-free catalytic DNA circuit for amplified detection of aflatoxin B1 using gold nanoparticles as colorimetric indicators†

Junhua Chen,* Junlin Wen, Li Zhuang and Shungui Zhou*

An enzyme-free biosensor for the amplified detection of aflatoxin B1 has been constructed based on a catalytic DNA circuit. Three biotinylated hairpin DNA probes (H1, H2, and H3) were designed as the assembly components to construct the sensing system (triplex H1–H2–H3 product). Cascaded signal amplification capability was obtained through toehold-mediated strand displacement reactions to open the hairpins and recycle the trigger DNA. By the use of streptavidin-functionalized gold nanoparticles as the signal indicators, the colorimetric readout can be observed by the naked eye. In the presence of a target, the individual nanoparticles (red) aggregate into a cross-linked network of nanoparticles (blue) *via* biotin–streptavidin coupling. The colorimetric assay is ultrasensitive, enabling the visual detection of trace levels of aflatoxin B1 (AFB1) as low as 10 pM without instrumentation. The calculated limit of detection (LOD) is 2 pM in terms of 3 times standard deviation over the blank response. The sensor is robust and works even when challenged with complex sample matrices such as rice samples. Our sensing platform is simple and convenient in operation, requiring only the mixing of several solutions at room temperature to achieve visible and intuitive results, and holds great promise for the point-of-use monitoring of AFB1 in environmental and food samples.

Received 18th February 2016,
Accepted 12th April 2016

DOI: 10.1039/c6nr01381c

www.rsc.org/nanoscale

Introduction

Aflatoxin B1 (AFB1), a secondary fungal metabolite of *Aspergillus flavus* and *Aspergillus parasiticus*, is one of the most frequently found mycotoxins in contaminated foods and has been classified as a group I carcinogen by the International Agency for Research on Cancer (IARC).[1] Many countries have established regulations to govern the AFB1 level in agricultural products. For example, the European Union has set up the maximum allowed level of AFB1 at 2 μg kg^{-1} for groundnuts, dried fruits, cereals, and milk.[2] Considering the low permissible limit, frequent occurrence, and high toxicity of AFB1, it is an urgent need to develop sensitive and on-site analytical methods for AFB1 monitoring to ensure food safety. In recent years, several elegant sensing strategies have been developed for AFB1 detection, including the immunoreaction technique,[2,3] electrochemical detectors,[4] and fluorescence sensors.[1,5] Despite significant contributions having been made to AFB1 monitoring, most of them require professional laboratory conditions, expensive instrumentation, and complicated washing procedures, which limit the in-field detection and point-of-use applications. Thus, it is highly desirable to develop an on-site biosensor for AFB1 detection without instrumentation.

Colorimetric biosensors using gold nanoparticles as the signal reporters have attracted increasing attention for mycotoxin determination because of their advantages of simplicity, ease of use, miniaturization, and on-site analysis.[6a–e] Detectors coupled with gold nanoparticles provided a promising sensing platform for target analysis based on their remarkably high extinction coefficient and strongly distance-dependent optical properties.[6f] The aggregation-induced, red-to-blue color change associated with gold nanoparticles is perhaps one of the most powerful and simple nanosensing methods available.[6g,h] The colorimetric readout can be visualized by the naked eye without requiring additional instrumentation.[6i] However, they often suffer from low sensitivity, especially in the detection of real samples. One way to improve the sensitivity is through signal amplification. Several groups have employed polymerase,[5c,7a] nicking endonuclease,[7b] and exonuclease[7c] to amplify the mycotoxin detection signals. Although these techniques can quantify even trace amounts of mycotoxins, all of them necessitate protein enzymes for signal amplification,

Guangdong Key Laboratory of Agricultural Environment Pollution Integrated Control, Guangdong Institute of Eco-Environmental and Soil Sciences, Guangzhou 510650, China. E-mail: jhchen@soil.gd.cn, sgzhou@soil.gd.cn; Fax: +86 20 8702 5872; Tel: +86 20 3730 0951

† Electronic supplementary information (ESI) available: Experimental details and additional data. See DOI: 10.1039/c6nr01381c

which increase the cost and complexity. As an alternative, toehold-mediated DNA strand displacement reaction has been proven to be a powerful mechanism for signal amplification without enzymes.[8] This nonenzymatic DNA self-assembly process can take place at room temperature without requiring a thermal annealing step. Owing to its predictable thermodynamics and kinetics, continuous signal turnover capability, and inherent modularity, this concept has been successfully applied to the construction of chemical amplifiers,[9] logic gates,[10] and molecular machines.[11] However, to date, little attention has been paid to employing enzyme-free amplified sensors for the analysis of mycotoxins. To explore new applications of the toehold-mediated strand displacement, we developed an enzyme-free catalytic DNA circuit for AFB1 detection with cascaded signal amplification using gold nanoparticles as the signal indicators. The simplicity of this assay should make it more convenient than our previously reported methods that use G-quadruplex DNAzyme as a catalytic unit to oxidize the H_2O_2–TMB system for the signal readout or SYBR Green I for fluorescent results.[9b,c] In general, assay methods that can detect mycotoxins with the naked eye without resorting to any instrumentation are convenient, and, for this reason, an assay integrating enzyme-free catalytic DNA circuit and gold nanoparticles for AFB1 detection would be of great interest.

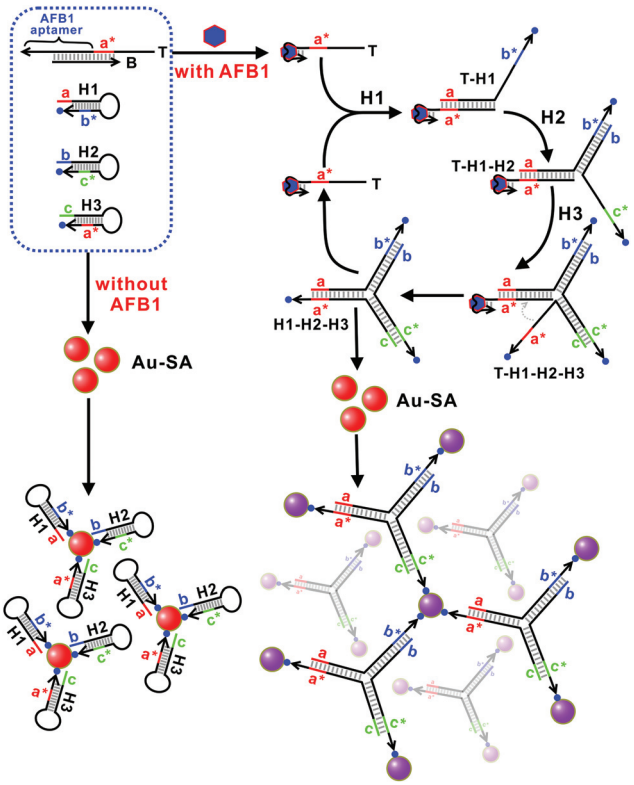

Scheme 1 Schematic illustration of the design strategy for the amplified detection of AFB1 on the basis of a catalytic DNA circuit and gold nanoparticles. Biotinylated hairpins (H1, H2, and H3) were used to construct the sensing system for cascaded signal amplification (the DNA sequences were listed in Table S1, ESI†). Streptavidin-functionalized gold nanoparticles (Au–SA) were used as colorimetric indicators. Arrows drawn on DNA strands represent 3 termini. Toeholds and toehold binding domains are named by letters and complementarity is denoted by asterisks.

Results and discussion

Design strategy for visual AFB1 detection

The design strategy for the amplified detection of AFB1 on the basis of a catalytic DNA circuit and gold nanoparticles is illustrated in Scheme 1.

The AFB1 aptamer-based trigger DNA (T) was inhibited by a blocking DNA (B). In the absence of AFB1, the trigger DNA failed to initiate the catalytic DNA circuit because the toehold domain a* is inaccessible. When the target (AFB1) binds to the aptamer, the T–B duplex is destabilized and a* is available to activate the following cascaded signal amplification. The exposed domain a* of the trigger strand first nucleates at the segment a of hairpin H1, mediating a branch migration that opens H1 and forms a T–H1 intermediate. In the T–H1 intermediate, domain b* of H1 is no longer occluded and binds to domain b of H2, again initiating a branch migration to form a T–H1–H2 complex where domain c* of H2 is open. Then, domain c of H3 can hybridize to the newly accessible toehold c* of H2, activating a strand displacement to open H3 and generate a T–H1–H2–H3 complex. This complex is inherently unstable, and T dissociates from the H1–H2–H3 complex, completing the reaction and allowing T to act as a catalyst to trigger the hybridization of additional hairpins. The process makes numerous biotinylated hairpins from singles to triplex (H1–H2–H3). After the addition of streptavidin-functionalized gold nanoparticles (Au–SA) into the sensing system, the biotinylated H1–H2–H3 product can interact with Au–SA *via* SA–biotin combination to form a cross-linked network of nanoparticles, which is blue in color due to the red-shifting and dampening of the nanoparticle plasmon resonance.[12] The resulting Au–SA aggregates can then be used as colorimetric indicators of AFB1 concentration. The red-to-blue color change can be visualized with the naked eye, or the absorbance can be measured by UV-vis spectroscopy. In the absence of a target, the trigger T should be catalytically inactive. The hairpins are kinetically impeded from forming the H1–H2–H3 complex. In this state, individual hairpins would not induce the assembly of Au–SA into cross-linked aggregates, thus a red color of dispersed gold nanoparticles could be observed.

Viability of the design

To demonstrate the viability of our design, the solutions at different conditions were analyzed by UV-vis spectroscopy, dynamic light scattering (DLS) and transmission electron microscopy (TEM). As shown in Fig. 1A, in the absence of AFB1, a narrow absorption peak at 520 nm for dispersed Au–SA was observed, and the color of the solution was red (inset in Fig. 1A), indicating that the monomer hairpins are metastable and cannot initiate the DNA self-assembly without a target. On the other hand, when AFB1 was added into the sensing

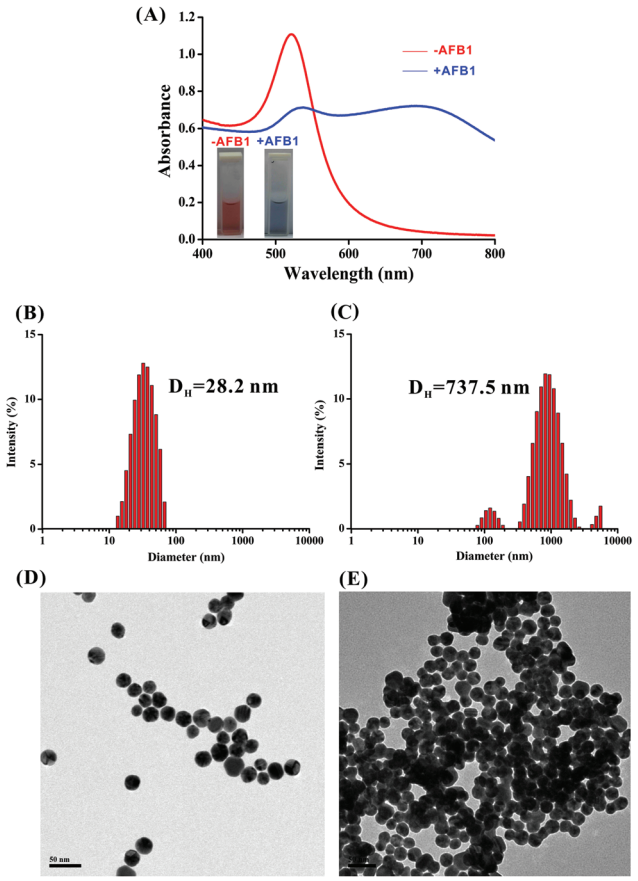

Fig. 1 (A) UV-vis absorption spectra of the colorimetric detection system in the absence and presence of AFB1 (1 μM). Inset: photographs of AFB1-induced color change of the Au–SA dispersion. (B) DLS measured hydrodynamic size distribution of Au–SA. (C) DLS measured hydrodynamic size distribution of the Au–SA assembly in the presence of 1 μM AFB1. (D) TEM image of the dispersed Au–SA. (E) TEM image of a microscopic Au–SA assembly in the presence of 1 μM AFB1. Scale bar: 50 nm.

system, a broad absorption for the Au–SA aggregates appeared at 650–700 nm, and the absorbance at 520 nm decreased (Fig. 1A). Correspondingly, the color of the solution changed from red to blue (inset in Fig. 1A). Further evidence for the AFB1 induced aggregation of Au–SA was supported by DLS results and TEM images. DLS analysis revealed the average hydrodynamic diameter of Au–SA to be around 28.2 nm (Fig. 1B). TEM micrographs showed that the particles were almost spherical and well dispersed with a narrow size in the range of 17–23 nm (Fig. 1D). The DLS measured size of Au–SA is slightly larger than the TEM measured value as expected due to the fact that DLS provides the hydrodynamic diameter, measured from the random thermodynamic motion of the particles (Brownian motion), which is greater than the actual size of the particles.[13] Upon addition of 1 μM target AFB1, the average hydrodynamic diameter of Au–SA increased to 737.5 nm (Fig. 1C). The formation of large DNA-linked three-dimensional aggregates in the presence of AFB1 can be clearly observed from the TEM image (Fig. 1E), revealing that the target-triggered self-assembly reaction had taken place, which was in good agreement with the DLS signal. AFB1 can trigger a cascade of hairpin hybridization events to yield numerous three-arm branched junctions (H1–H2–H3), which interact with Au–SA to form a cross-linked network of nanoparticles, inducing the aggregation of Au–SA. The arm length for the 3-arm junction is calculated to be 7.8 nm.[8a] When two nanoparticles are brought into proximity (within about 2.5 times the particle diameter) their plasmons couple in a distance-dependent manner.[14] As the interparticle distance decreases, the coupled plasmon resonance wavelength red-shifts.[12a,15] In the presence of AFB1, the interparticle distance of Au–SA will decrease due to the formation of multiple tethers (3-arm junctions) between the nanoparticles. Thus, the plasmon resonance peak wavelengths of these formed three-dimensional aggregates are significantly red-shifted in comparison with that of the single Au–SA nanoparticle. The DLS experiments and TEM results show that the spectrum shift and color change of the solution are associated with the degree of particle aggregation.

Optimization of assay conditions

As the trigger DNA T can competitively hybridize with both the blocking DNA B and target AFB1, the molar ratio of T to B is a key factor to influence the sensing process. We fixed the concentration of T and changed the concentration of B to obtain the different ratios of 1 : 1, 1 : 2, 1 : 3, 1 : 4, and 1 : 5. As shown in Fig. 2, the levels of signal increase were calculated to be 62%, 80%, 118%, 104%, and 75%, respectively. With higher molar ratios, too much B would induce an insufficient displacement between AFB1 and T, which subsequently affected the quantity of product H1–H2–H3 created in the catalytic DNA circuit. With lower molar ratios, a deficient amount of B would

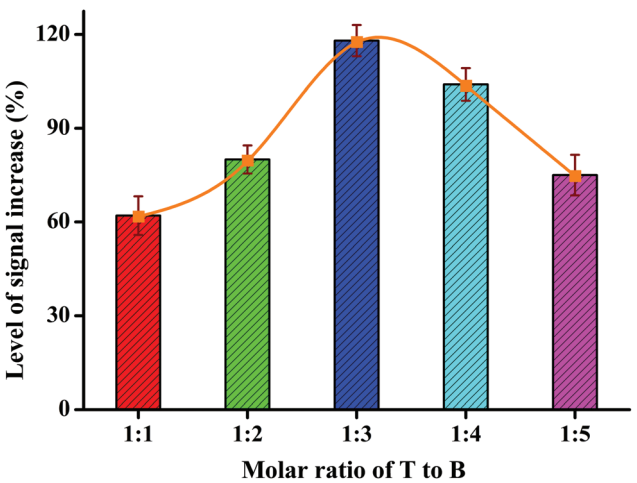

Fig. 2 Effect of the molar ratio of T to B on the response of the sensing system. The level of signal increase was plotted as a function of the molar ratio. Level of signal increase = $(S - N)/N \times 100\%$, where S is the signal triggered by 10 nM AFB1 and N is the signal of the corresponding negative control in the absence of AFB1. T: 100 nM, hairpin DNA: 600 nM.

result in low hybridization efficiency between T and B and lead to a high background signal. Therefore, the ratio of 1 : 3 was selected for target detection.

The process of signal amplification was strongly affected by the incubation time of the hairpins for DNA self-assembly. Real-time monitoring of the dynamic assembly of the catalytic DNA circuit was performed. From the start of the assembly reaction, the resulting absorption intensity was recorded every several minutes. As shown in Fig. 3, the absorption ratio (A_{650}/A_{520}) of the sensing system increased gradually along with the assembly time in the presence of the target AFB1, and kept almost a constant level after 90 min (red circle in Fig. 3), which indicated that the reaction equilibrium was reached. However, the ratio of the background test maintained its increase even after 90 min (black circle in Fig. 3). Since the target-catalyzed assembly of branched junctions from hairpin DNA is a kinetically controlled process, it was possible that prolonged incubation times could cause more leaks and increased background signals. Therefore, for the best signal-to-noise level, 90 min of assembly time was selected in future experiments.

We also studied the influence of the concentration of hairpins (H1, H2, and H3) on the colorimetric response of the system, since the hairpins were not only the building blocks for constructing the sensing circuit but also functioned in the Au–SA aggregation. As shown in Fig. 4, with the increase of the concentrations of the hairpin DNA, the absorption ratio (A_{650}/A_{520}) of the solution containing 10 nM AFB1 increased gradually and reached a plateau at 600 nM hairpins (red histogram). However, in the absence of AFB1, the A_{650}/A_{520} ratio also increased slowly with increasing hairpin concentrations (black histogram). Thus, in order to achieve the highest net signal (blue histogram), 600 nM hairpin DNA was selected for the subsequent experiments.

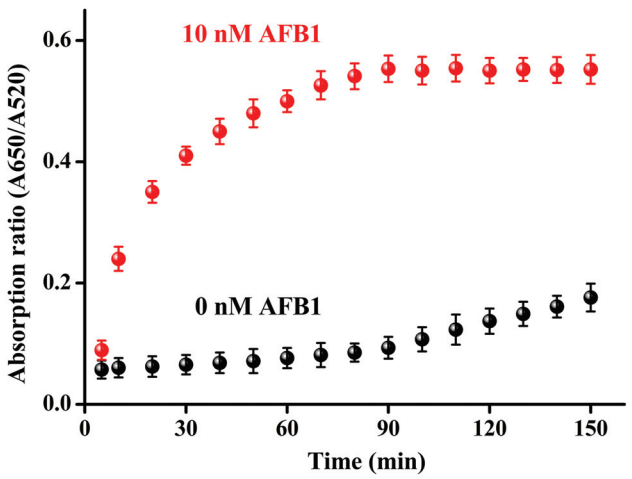

Fig. 3 Real-time monitoring of the changes in the absorption ratio (A_{650}/A_{520}) of the sensing system in the presence of 10 nM AFB1 (red circle) or with no target AFB1 (black circle). The experiments were performed at room temperature (~25 °C). T: 100 nM, B: 300 nM, hairpin DNA: 600 nM.

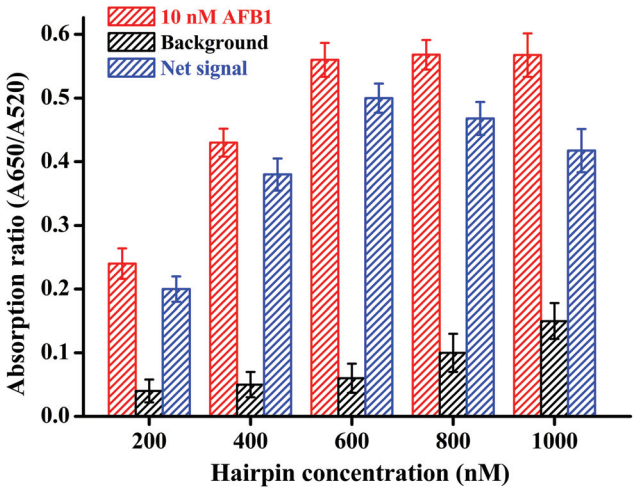

Fig. 4 Effect of the concentration of the hairpins on the colorimetric response. The absorption ratio (A_{650}/A_{520}) was plotted as a function of the concentration of the hairpins in the presence of 10 nM AFB1 (red histogram) and in the absence of AFB1 (black histogram), respectively. Net signal (blue histogram) = $(A_{650}/A_{520})_{\text{with AFB1}} - (A_{650}/A_{520})_{\text{without AFB1}}$. T: 100 nM, B: 300 nM.

In order to achieve a better sensing performance, the pH value of the system was also optimized. As shown in Fig. 5, the absorption ratio (A_{650}/A_{520}) of the solution containing 10 nM AFB1 improved sharply when the pH increased from 5.0 to 7.0, and then reached a relatively stable level with the pH ranging from 7.0 to 8.0. Meanwhile, the absorption ratio decreased as the pH further increased. To obtain the best performance of the sensing system for AFB1 monitoring, a pH of 7.4 was selected as the optimal pH condition for all succeeding experiments. A search was also conducted to identify the suitable buffer composition for AFB1 monitoring (Fig. S1, ESI†). The optimal reaction buffer is 10 mM Tris-HCl, 120 mM NaCl, 5 mM KCl, 5 mM $MgCl_2$, pH 7.4.

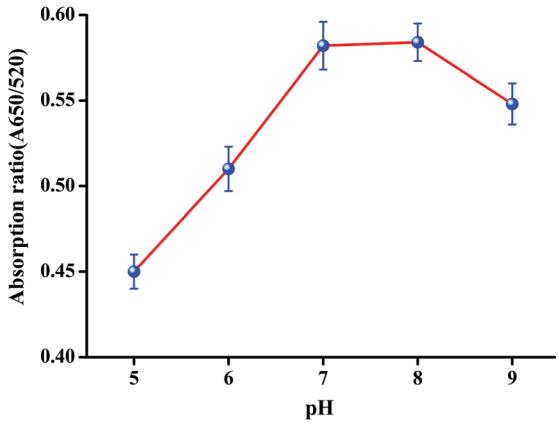

Fig. 5 Effect of the pH value on the sensing performance of the biosensor. AFB1 concentration: 10 nM. T: 100 nM, B: 300 nM, hairpin DNA: 600 nM. The experiments were performed at room temperature (~25 °C).

Analytical performance for AFB1 detection

To investigate the detection ability of this colorimetric method, different concentrations of AFB1 were tested under the optimal experimental conditions. As shown in Fig. 6A, with the increase of AFB1 concentration, the color of gold nanoparticles was gradually changed from red to blue, implying that the Au–SA was assembled into a larger cross-linked network of nanoparticles in the presence of higher AFB1 concentrations. Meanwhile, in the UV-vis spectra, the absorbance at 520 nm gradually shifted and decreased, while the absorbance at 650 nm correspondingly increased (Fig. 6B). The ratio between the absorbance at 650 nm and 520 nm (A_{650}/A_{520}) continued to increase upon increasing AFB1 concentration until a plateau was reached (Fig. 6C). The resulting calibration curve showed that the absorbance ratios were linear to the logarithm of AFB1 concentrations in the range from 10 pM to 1 μM (Fig. 6C, inset). This colorimetric assay allowed for the detection of AFB1 at a concentration as low as 10 pM by the naked eye. The calculated limit of detection (LOD) is 2 pM. The LOD is defined by $3S_0/S$,[9c,16] where 3 is the factor at the 99% confidence level, S_0 is the standard deviation of the blank measurements (n = 12), and S is the slope of the calibration curve. The detection limit of our sensing strategy is about 2 orders of magnitude better than the previously reported gold nanoparticle-based sensor for AFB1 without signal amplification.[6c] The detection capability is comparable to or even better than some previously reported sensors for AFB1 detection.[1,4c,5a,c] This high sensitivity can be primarily attributed to the continuous turnover capability of the enzyme-free catalytic DNA circuit. As the maximum permissible limit of AFB1 in groundnuts, dried fruits, cereals, and milk was set by the European Union to be 2 ng mL^{-1} (64 nM), our proposed biosensor is promising for the on-site detection of AFB1 with a superior detection limit and large dynamic range.

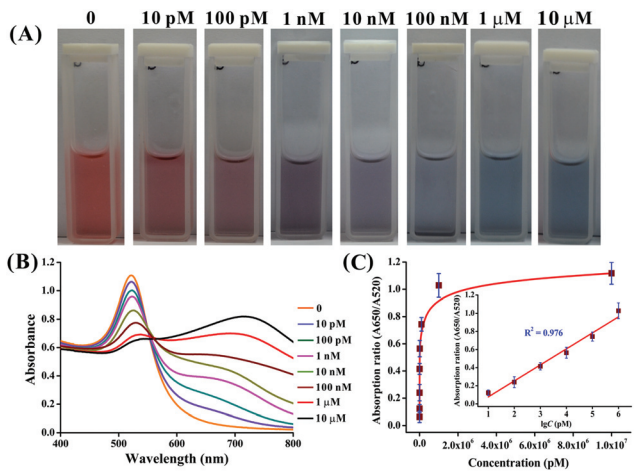

Fig. 6 (A) Photographs showing colorimetric responses of the detection system in the presence of various concentrations of AFB1. (B) Their corresponding UV-vis absorbance spectra. (C) Plots of absorption ratios (A_{650}/A_{520}) *versus* the concentration of AFB1. Inset shows the calibration curve for concentrations ranging from 10 pM to 1 μM. The error bars indicate the standard deviations of three replicates.

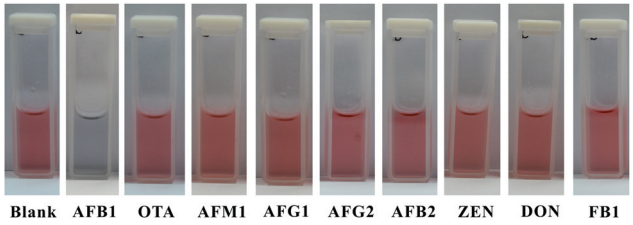

Fig. 7 Visual observation of the color change of the colorimetric system treated with 100 nM AFB1 and 1 μM other mycotoxins.

Selectivity and real sample analysis

The selectivity of this colorimetric biosensor for AFB1 was examined by a visual assay to other mycotoxins, including ochratoxin A (OTA), aflatoxin M1 (AFM1), aflatoxin G1 (AFG1), aflatoxin G2 (AFG2), aflatoxin B2 (AFB2), zearalenone (ZEN), deoxynivalenol (DON), and fumonisin (FB1). As shown in Fig. 7, the color of the solution turned to blue only in the presence of AFB1 (100 nM), resulting from the aggregation of the cross-linked network of nanoparticles. However, other control mycotoxins at a concentration of 1 μM did not induce any obvious color change compared with the blank sample. The above results clearly demonstrated that our developed method exhibited excellent specificity for the detection of AFB1. Such a high selectivity of this assay can be attributed to the specific aptamer–ligand interaction.

To evaluate the practical applicability and accuracy of this method, it was validated by the analysis of AFB1 in rice samples. The samples spiked with various concentrations of AFB1 were detected according to the general procedure with three replicates. The results of the determination are listed in Table S2 (ESI†). Satisfactory recoveries were obtained in the range of 90–112% with acceptable relative standard deviation (RSD). These results demonstrated that the established sensing system could be used for AFB1 monitoring in real agriculture products.

Conclusions

In conclusion, we have successfully developed a colorimetric assay for the amplified detection of AFB1 using a catalytic DNA circuit for cascaded signal amplification. The working principle is based on a series of toehold-mediated strand displacement reactions, which can take place at room temperature without any enzyme. Three biotinylated hairpin probes (H1, H2, and H3) were utilized as the building blocks to construct the sensing platform (triplex H1–H2–H3 product). By the use of Au–SA as a signal transducer, the target solution with a concomitant red-to-blue color change can be recognized readily by the naked eye. The colorimetric biosensor is ultrasensitive for AFB1 detection, with a detection limit of 2 pM,

which is about 2 orders of magnitude better than the previously reported gold nanoparticle-based sensor without signal amplification. In addition, our approach shows excellent selectivity for AFB1 against other mycotoxins. This sensor is robust and can be applied to the reliable detection of spiked AFB1 in rice samples with satisfactory recovery and accuracy. Importantly, our method is simple in operation, requiring only the mixing of several solutions at room temperature to achieve visible and intuitive results, and holds great promise in on-site applications. Furthermore, this assay can be adapted easily to a high-throughput and automatic screening format. Significantly, the enzyme-free catalytic DNA circuit can be easily extended for the determination of other small molecules by simply substituting the target-specific aptamer sequence, thus giving a versatile sensing platform.

Acknowledgements

Financial support was provided by the National Natural Science Foundation of China (Grant No. 21407029), the Pearl River S&T Nova Program of Guangzhou (Grant No. 201506010093), the Natural Science Foundation of Guangdong Province (Grant No. 2014A030313705), the Science and Technology Program of Guangzhou (Grant No. 201508020010), and the Key Projects in the National Science & Technology Pillar Program of China (Grant No. 2015BAD06B03).

Notes and references

1 W. Shim, M. J. Kim, H. Mun and M. Kim, *Biosens. Bioelectron.*, 2014, **62**, 288–294.
2 (*a*) W. Xu, Y. Xiong, W. Lai, Y. Xu, C. Li and M. Xie, *Biosens. Bioelectron.*, 2014, **56**, 144–150.
3 (*a*) A. Pal and T. K. Dhar, *Anal. Chem.*, 2004, **76**, 98–104; (*b*) X. Xu, X. Liu, Y. Li and Y. Ying, *Biosens. Bioelectron.*, 2013, **47**, 361–367; (*c*) X. Jin, X. Jin, L. Chen, J. Jiang, G. Shen and R. Yu, *Biosens. Bioelectron.*, 2009, **24**, 2580–2585; (*d*) X. Wang, J. Pauli, R. Niessner, U. Resch-Genger and D. Knopp, *Analyst*, 2015, **140**, 7305–7312; (*e*) X. Wang, R. Niessner and D. Knopp, *Analyst*, 2015, **140**, 1453–1458.
4 (*a*) D. Wang, W. Hu, Y. Xiong, Y. Xu and C. M. Li, *Biosens. Bioelectron.*, 2015, **63**, 185–189; (*b*) G. Evtugyn, A. Porfireva, V. Stepanova, R. Sitdikov, I. Stoikov, D. Nikolelis and T. Hianik, *Electroanalysis*, 2014, **26**, 2100–2109; (*c*) Y. Lin, Q. Zhou, Y. Lin, D. Tang, G. Chen and D. Tang, *Biosens. Bioelectron.*, 2015, **74**, 680–686.
5 (*a*) M. Ren, H. Xu, X. Huang, M. Kuang, Y. Xiong, H. Xu, Y. Xu, H. Chen and A. Wang, *ACS Appl. Mater. Interfaces*, 2014, **6**, 14215–14222; (*b*) Z. Lu, X. Chen, Y. Wang, X. Zheng and C. M. Li, *Microchim. Acta*, 2015, **182**, 571–578; (*c*) X. Guo, F. Wen, N. Zheng, Q. Luo, H. Wang, H. Wang, S. Li and J. Wang, *Biosens. Bioelectron.*, 2014, **56**, 340–344.
6 (*a*) S. Song, N. Liu, Z. Zhao, E. N. Ediage, S. Wu, C. Sun, S. D. Saeger and A. Wu, *Anal. Chem.*, 2014, **86**, 4995–5001; (*b*) Z. Mei, H. Chu, W. Chen, F. Xue, J. Liu, H. Xu, R. Zhang and L. Zheng, *Biosens. Bioelectron.*, 2013, **39**, 26–30; (*c*) Y. Luan, Z. Chen, G. Xie, J. Chen, A. Lu, C. Li, H. Fu, Z. Ma and J. Wang, *J. Nanosci. Nanotechnol.*, 2015, **15**, 1357–1361; (*d*) R. Liu, Y. Huang, Y. Ma, S. Jia, M. Gao, J. Li, H. Zhang, D. Xu, M. Wu, Y. Chen, Z. Zhu and C. Yang, *ACS Appl. Mater. Interfaces*, 2015, **7**, 6982–6990; (*e*) C. Yang, Y. Wang, J. Marty and X. Yang, *Biosens. Bioelectron.*, 2011, **26**, 2724–2727; (*f*) R. Wilson, *Chem. Soc. Rev.*, 2008, **37**, 2028–2045; (*g*) J. Lee, M. S. Han and C. A. Mirkin, *Angew. Chem., Int. Ed.*, 2007, **46**, 4093–4096; (*h*) J. Lee, P. A. Ulmann, M. S. Han and C. A. Mirkin, *Nano Lett.*, 2008, **8**, 529–533; (*i*) M. S. Han, A. K. R. Lytton-Jean, B. Oh, J. Heo and C. A. Mirkin, *Angew. Chem., Int. Ed.*, 2006, **45**, 1807–1810.
7 (*a*) L. Huang, J. Wu, L. Zheng, H. Qian, F. Xue, Y. Wu, D. Pan, S. B. Adeloju and W. Chen, *Anal. Chem.*, 2013, **85**, 10842–10849; (*b*) X. Hun, F. Liu, Z. Mei, L. Ma, Z. Wang and X. Luo, *Biosens. Bioelectron.*, 2013, **39**, 145–151; (*c*) P. Tong, L. Zhang, J. Xu and H. Chen, *Biosens. Bioelectron.*, 2011, **29**, 97–101.
8 (*a*) P. Yin, H. M. T. Choi, C. R. Calvert and N. A. Pierce, *Nature*, 2008, **451**, 318–323; (*b*) D. Y. Zhang and G. Seelig, *Nat. Chem.*, 2011, **3**, 103–113; (*c*) D. Y. Zhang and E. Winfree, *J. Am. Chem. Soc.*, 2009, **131**, 17303–17314; (*d*) L. Qian and E. Winfree, *Science*, 2011, **332**, 1196–1201.
9 (*a*) R. Duan, B. Wang, F. Hong, T. Zhang, Y. Jia, J. Huang, A. Hakeem, N. Liu, X. Lou and F. Xia, *Nanoscale*, 2015, **7**, 5719–5725; (*b*) J. Chen, J. Wen, G. Yang and S. Zhou, *Chem. Commun.*, 2015, **51**, 12373–12376; (*c*) J. Chen and S. Zhou, *Biosens. Bioelectron.*, 2016, **77**, 277–283; (*d*) F. Xuan and I. Hsing, *J. Am. Chem. Soc.*, 2014, **136**, 9810–9813; (*e*) H. Zhang, F. Li, B. Dever, X. Li and X. C. Le, *Chem. Rev.*, 2013, **113**, 2812–2841.
10 (*a*) K. He, Y. Li, B. Xiang, P. Zhao, Y. Hu, Y. Huang, W. Li, Z. Niu and S. Yao, *Chem. Sci.*, 2015, **6**, 3556–3564; (*b*) Y. Guo, J. Wu and H. Ju, *Chem. Sci.*, 2015, **6**, 4318–4323; (*c*) J. Chen, S. Zhou and J. Wen, *Angew. Chem., Int. Ed.*, 2015, **54**, 446–450; (*d*) M. You, G. Zhu, T. Chen, M. J. Donovan and W. Tan, *J. Am. Chem. Soc.*, 2015, **137**, 667–674; (*e*) J. Elbaz, O. Lioubashevski, F. Wang, F. Remacle, R. D. Levine and I. Willner, *Nat. Nanotechnol.*, 2010, **5**, 417–422.
11 (*a*) F. Wang, X. Liu and I. Willner, *Angew. Chem., Int. Ed.*, 2015, **54**, 1098–1129; (*b*) F. Wang, C. Lu and I. Willner, *Chem. Rev.*, 2014, **114**, 2881–2941; (*c*) T. Song, S. Xiao, D. Yao, F. Huang, M. Hu and H. Liang, *Adv. Mater.*, 2014, **26**, 6181–6185; (*d*) Y. Chen, N. Dalchau, N. Srinivas, A. Phillips, L. Cardelli, D. Soloveichik and G. Seelig, *Nat. Nanotechnol.*, 2013, **8**, 755–762; (*e*) C. E. Castro, H. Su, A. E. Marras, L. Zhou and J. Johnson, *Nanoscale*, 2015, **7**, 5913–5921.
12 (*a*) R. Elghanian, J. J. Storhoff, R. C. Mucic, R. L. Letsinger and C. A. Mirkin, *Science*, 1997, **277**, 1078–1081; (*b*) G. Song, C. Chen, J. Ren and X. Qu, *ACS Nano*, 2009, **3**, 1183–1189; (*c*) C. Chen, C. Zhao, X. Yang, J. Ren and X. Qu, *Adv. Mater.*, 2010, **22**, 389–393; (*d*) W. Zhou, X. Gao, D. Liu and X. Chen, *Chem. Rev.*, 2015, **115**, 10575–10636.

13 (*a*) R. Finsy, *Adv. Colloid Interface Sci.*, 1994, **52**, 79–143; (*b*) O. A. Alsager, S. Kumar, G. R. Willmott, K. P. McNatty and J. M. Hodgkiss, *Biosens. Bioelectron.*, 2014, **57**, 262–268.
14 K. H. Su, Q. H. Wei, X. Zhang, J. J. Mock, D. R. Smith and S. Schultz, *Nano Lett.*, 2003, **3**, 1087–1090.
15 B. M. Reinhard, M. Siu, H. Agarwal, A. P. Alivisatos and J. Liphardt, *Nano Lett.*, 2005, **5**, 2246–2252.
16 (*a*) F. H. Hernandez and J. M. Escriche, *Analyst*, 1984, **109**, 1585–1588; (*b*) J. Chen and L. Zeng, *Biosens. Bioelectron.*, 2013, **42**, 93–99.